The Astrophysical Journal Supplement Series, 241:6 (15pp), 2019 March https://doi.org/10.3847/1538-4365/ab01fe

Searching for Super-fast Rotators Using the Pan-STARRS 1

Chan-Kao Chang[1], Hsing-Wen Lin[1,2], Wing-Huen Ip[1,3], Wen-Ping Chen[1], Ting-Shuo Yeh[1], K. C. Chambers[4], E. A. Magnier[4], M. E. Huber[4], H. A. Flewelling[4], C. Z. Waters[4], R. J. Wainscoat[4], and A. S. B. Schultz[4]
[1] Institute of Astronomy, National Central University, Jhongli, Taiwan; rex@astro.ncu.edu.tw
[2] Department of Physics, University of Michigan, Ann Arbor, MI 48109, USA
[3] Space Science Institute, Macau University of Science and Technology, Macau
[4] Institute for Astronomy, University of Hawaii, Honolulu, HI 96822, USA
Received 2018 September 28; revised 2019 January 22; accepted 2019 January 24; published 2019 February 28

Abstract

A class of asteroids, called large super-fast rotators (large SFRs), have rotation periods shorter than 2 hr and diameters larger than ~0.3 km. They pose challenges to the usual interior rubble-pile structure unless a relatively high bulk density is assumed. So far, only six large SFRs have been found. Therefore, we present a survey of asteroid rotation periods using the Panoramic Survey Telescope and Rapid Response System (Pan-STARRS) 1 telescope during 2016 October 26–31 to search for more large SFRs and to study their properties. A total of 876 reliable rotation periods are measured, among which seven are large SFRs, thereby increasing the inventory of known large SFRs. These seven newly discovered large SFRs have diverse colors and locations in the main asteroid belt, suggesting that the taxonomic tendency and the location preference in the inner main belt of the six previously known large SFRs could be a bias due to various observational limits. Interestingly, five out of the seven newly discovered large SFRs are mid main-belt asteroids (MBAs). Considering the rare discovery rates of large SFR in the previously similar surveys and the survey condition in this work, the chance of detecting a large SFR in the inner main belt seems to be relatively low. This probably suggests that the inner main belt harbors fewer large SFRs than the mid main belt. From our survey, we also found a drop in the number appearing at $f > 5\,\mathrm{rev\,day^{-1}}$ on the spin-rate distribution for the outer MBAs of $D < 3$ km, which was reported for the inner and mid main belt by Chang et al.

Key words: minor planets, asteroids: general – surveys

Supporting material: figure set, machine-readable table

1. Introduction

Asteroid time-series study was a relatively unexplored field in planetary science because it was a challenge to collect a large number of asteroid light curves within a short period of time. Thanks to the significant advance in observational technology (i.e., robotic telescopes and wide-field cameras) and information science (i.e., high computing power and massive storage), such a challenge becomes accessible, and asteroid time-series study can, therefore, be conducted in a more comprehensive way through wide-field surveys in the last decade (Masiero et al. 2009; Polishook & Brosch 2009; Dermawan et al. 2011; Polishook et al. 2012; Chang et al. 2014a, 2015, 2016; Waszczak et al. 2015).

The 2 hr spin barrier (Harris 1996; Pravec et al. 2002) has continuously been found for asteroids mostly with a size of a few hundred meters or larger, collected from these wide-field surveys. Moreover, the relation between the spin-rate limit and the bulk density of asteroids in this size range (i.e., $P \sim 3.3\sqrt{(1+\Delta m)/\rho}$; Harris 1996) shows for the first time in these data sets that the S-type asteroids have higher spin-rate limits than the C-type asteroids (Chang et al. 2015; Waszczak et al. 2015). This suggests that the rubble-pile structure (i.e., gravitationally bounded aggregation) is generally applicable to these asteroids. However, six large super-fast rotators (SFRs) (i.e., $D > 300$ m) have been found to break the 2 hr spin barrier and challenged the rubble-pile structure (SFRs; see Table 2 in Chang et al. 2017, and references therein). Although internal cohesion (Holsapple 2007; Sánchez & Scheeres 2012) is a possible solution to keep these large SFRs intact under their super-fast rotations, the rarity of large SFRs, compared to the average asteroids, somehow suggest that cohesion might be only available to certain asteroids. Moreover, a taxonomic tendency seems present in the six known large SFRs (Chang et al. 2017). If the aforementioned rarity of large SFR and the taxonomic tendency are true, large SFRs could just possibly be a special group distinguished from the average asteroids. Therefore, any preference shared by large SFRs, such as composition, size, and location in the main asteroid belt, is important to understand their nature.

The asteroid spin-rate distribution reflects the overall evolution of the spin state for a group of asteroids. Two dominant mechanisms, mutual collisions and the Yarkovsky–O'Keefe–Radzievskii–Paddack effect (YORP; Rubincam 2000), are believed to alter the spin states of main-belt asteroids (MBAs) effectively. While the former (i.e., collision equilibrium) would lead to a Maxwellian spin-rate distribution (Salo 1987), the latter tends to deviate the distribution from a Maxwellian form (Pravec et al. 2008). Indeed, asteroids with diameters larger than 40 km were shown to have a Maxwellian spin-rate distribution (Pravec & Harris 2000), and, contrarily, smaller asteroids display a distribution different from a Maxwellian form. Interestingly, some differences have been seen between the spin-rate distributions of smaller asteroids obtained from the target observations (i.e., a flat distribution; Pravec et al. 2008) and the wide-field surveys (i.e., a deviated Maxwellian form; Masiero et al. 2009; Chang et al. 2015, 2016; Waszczak et al. 2015); however, how this discrepancy was caused still needs more study. Because the timescales of both aforementioned mechanisms depend on the size and location of the asteroid (McNeill et al. 2016, and the references therein), some footprints are, therefore, expected to be

Table 1
Observation Information

Field No.	[R.A., Decl.] (°, °)	2016 Oct 26 Δt, $N_{\rm exp}$	2016 Oct 27 Δt, $N_{\rm exp}$	2016 Oct 28 Δt, $N_{\rm exp}$	2016 Oct 29 Δt, $N_{\rm exp}$	2016 Oct 30 Δt, $N_{\rm exp}$	2016 Oct 31 Δt, $N_{\rm exp}$
1	[28.10, 13.14]	6.8, 12	6.6, 32	6.5, 31	5.7, 25	6.9, 8	1.7, 8
2	[29.17, 10.33]	6.3, 11	6.6, 32	6.5, 31	5.7, 25	6.9, 8	1.7, 8
3	[31.00, 14.18]	6.8, 12	6.6, 32	6.5, 31	5.7, 25	6.9, 8	1.7, 7
4	[32.04, 11.36]	6.8, 12	6.6, 32	6.5, 31	5.7, 25	6.9, 8	1.7, 8
5	[33.92, 15.18]	6.8, 12	6.6, 32	6.5, 30	5.7, 25	6.9, 8	1.7, 7
6	[34.93, 12.35]	6.3, 11	6.6, 32	6.5, 31	5.7, 25	6.9, 8	1.7, 8
7	[36.87, 16.16]	6.8, 12	6.6, 32	6.5, 30	5.7, 25	6.9, 8	1.7, 7
8	[37.85, 13.31]	6.8, 12	6.6, 32	6.5, 31	5.7, 25	6.9, 8	1.7, 8

Note. Δt is the time duration spanned by each observing set in hrs, and $N_{\rm exp}$ is the total number of exposures for each night and field.

left in the spin-rate distributions. Fortunately, the recent wide-field surveys provide a good chance to study the spin-rate distributions of asteroids in different sizes and locations for further insight of asteroid spin-state altering mechanisms. Chang et al. (2015, 2016) found that the spin-rate distributions are similar for asteroids in a fixed diameter range at different locations. Besides, a drop in the number at $>5\,{\rm rev\,day}^{-1}$ was found in the spin-rate distributions for asteroids of $D < 3$ km in the inner and mid main belt, which was not seen for asteroids of $3 < D < 15$ km. The reason for this number drop is still unknown, and it is also interesting to know whether this number drop would also exist in the outer main belt.

To understand the aforementioned questions, a rotation period survey aimed at the kilometer-sized asteroids in the outer main belt is needed; therefore, we used the Panoramic Survey Telescope and Rapid Response System (Pan-STARRS) 1 (PS1) telescope to conduct a survey for an asteroid rotation period in 2016 October. From the survey, 876 reliable rotation periods were obtained and seven of them are large SFRs. The observation information and light-curve extraction are given in the Section 2. The rotation period analysis is described in Section 3. The results and discussion can be found in Section 4, and the summary and conclusion are presented in Section 5.

2. Observations and Data Reduction

The PS1 was designed to explore the visible 3π sky and is mainly dedicated to finding small solar system bodies, especially those potentially hazardous objects. The telescope is a 1.8 m RitcheyChretien reflector located on Haleakala, Maui, which is equipped with the Gigapixel Camera #1 to create a field of view of 7 deg^2. The available filters include g_{P1} (∼400–550 nm), r_{P1} (∼550–700 nm), i_{P1} (∼690–820 nm), z_{P1} (∼820–920 nm), and y_{P1} (>920 nm), and a special filter, w_{P1} (i.e., combination of g_{P1}, r_{P1}, and i_{P1}), was designed for the discovery of moving object (Kaiser et al. 2010; Tonry et al. 2012; Chambers et al. 2016).

In order to discover large SFRs and to carry out the spin-rate distribution of outer MBAs down to the kilometer size, we used the PS1 to conduct a special campaign to collect asteroid light curves in the w_{P1} band during 2016 October 26–31, in which eight consecutive PS1 fields (i.e., ∼56 deg^2 in total) over the ecliptic plane around the opposition were continuously scanned using a cadence of ∼10 minutes. In the first night of the campaign, we used an observation sequence of w_{P1}, g_{P1}, w_{P1}, r_{P1}, w_{P1}, i_{P1}, w_{P1}, and z_{P1} bands to obtain asteroid colors, and the other nights were only observed in the w_{P1} band. The exposure times for g_{P1}, r_{P1}, i_{P1}, z_{P1}, and w_{P1} bands were 120, 120, 180, and 60 s, respectively, and this would give us a similar limiting magnitude of 22.5 mag at 5σ level for each band. However, only few exposures were obtained for the last two nights of the campaign due to bad weather. The details of the observation can be found in Tables 1 and 2.

Table 2
Color Observation on 2016 October 26

Field No.	w_{P1} $N_{\rm exp}$	g_{P1} Δt, $N_{\rm exp}$	r_{P1} Δt, $N_{\rm exp}$	i_{P1} Δt, $N_{\rm exp}$	z_{P1}
1	6.8, 12	5.4, 3	5.4, 3	5.4, 3	5.4, 3
2	6.3, 11	5.4, 3	5.4, 3	5.4, 3	5.4, 3
3	6.8, 12	5.4, 3	5.4, 3	5.4, 3	5.4, 3
4	6.8, 12	5.4, 3	5.4, 3	5.4, 3	5.4, 3
5	6.8, 12	5.4, 3	5.4, 3	5.4, 3	5.4, 3
6	6.3, 11	5.4, 3	5.4, 3	5.4, 3	5.4, 3
7	6.8, 12	5.4, 3	5.4, 3	5.4, 3	5.4, 3
8	6.8, 12	5.4, 3	5.4, 3	5.4, 3	5.4, 3

Note. Δt is the time duration spanned by each observing set in hrs, and $N_{\rm exp}$ is the total number of exposures for each night and field. The exposure time for g_{P1}, r_{P1}, i_{P1}, z_{P1}, and w_{P1} bands were 120, 120, 120, 180, and 60 s, respectively. The observation sequence was $w_{P1} - g_{P1} - w_{P1} - r_{P1} - w_{P1} - i_{P1} - w_{P1} - z_{P1}$.

All the images obtained in the campaign were processed by the Image Processing Pipeline (IPP), which includes image detrending, instrumental signature removal, object detecting, image warping, and photometric and astrometric calibration (the detailed description can be found in Chambers et al. 2016; Magnier et al. 2016a, 2016b, 2016c; Waters et al. 2016). The IPP also performs image subtraction to find transient detections and then passes them to the Pan-STARRS Moving Object Processing System to discover new moving objects (Denneau et al. 2013). From this campaign, more than 1500 asteroids were discovered and reported to the Minor Planet Center.

The light curves of asteroids, including the known and newly discovered, were extracted by matching the detections against the ephemerides obtained from the *JPL/HORIZONS*[5] system with a search radius of 2″ after removing the detections of stationary sources.

3. Rotation Period Analysis, Color Calculation, and Diameter Estimation

After correcting light-travel time and reducing both heliocentric, r, and geocentric, Δ, distances to 1 au for all light-curve

[5] https://ssd.jpl.nasa.gov/sbfind.cgi

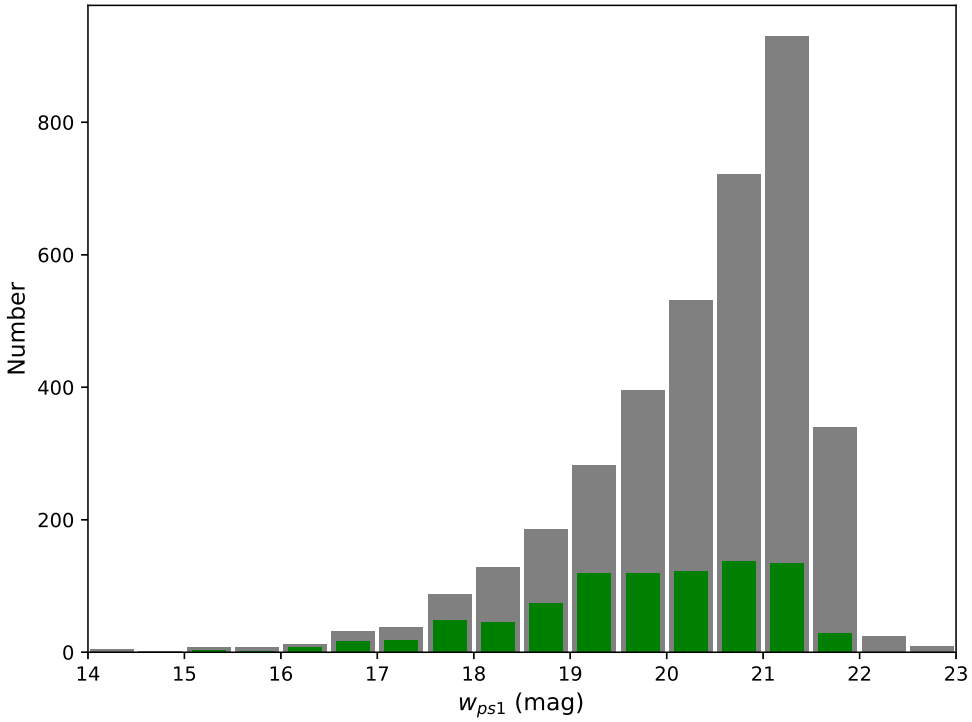

Figure 1. Magnitude distribution of asteroids observed in the survey. Green: asteroids with reliable rotation periods; gray: asteroids with 10 or more detections.

measurements, we fitted a second-order Fourier series to each light curve to find the rotation period (Harris et al. 1989):

$$M_{i,j} = \sum_{k=1}^{2} B_k \sin\left[\frac{2\pi k}{P}(t_j - t_0)\right] + C_k \cos\left[\frac{2\pi k}{P}(t_j - t_0)\right] + Z_i, \quad (1)$$

where $M_{i,j}$ are the reduced magnitudes in the w_{P1} band measured at the epoch, t_j; B_k and C_k are the coefficients in the Fourier series; P is the rotation period; and t_0 is an arbitrary epoch. We also introduced a constant value, Z_i, to correct the possible offsets in magnitude between the measurements obtained from different nights. The least-squares minimization was applied to Equation (1) to obtain the other free parameters for each given P, and the explored spin rate, $f = 1/P$, was from 0.25 to 50 rev day^{-1} with a step size of 0.01 rev day^{-1}. However, we excluded the upper and lower 5% of the detections in a light curve in the aforementioned fitting to avoid outliers, which might be contaminated by nearby bright stars or unknown sources.

A code (U), which describes the reliability of the derived rotation periods, was then assigned after a manual review for each light curve, where "3," "2," "1," and "0" mean highly reliable, some ambiguity, possibly correct, and no detection, respectively (Warner et al. 2009). We estimated the uncertainty of the rotation period using the frequency range that has χ^2 smaller than $\chi^2_{\rm best} + \triangle\chi^2$, where $\chi^2_{\rm best}$ is the χ^2 of the derived rotation period, and $\triangle\chi^2$ is the 68% (i.e., 1σ) of the inverse χ^2 distribution, assuming $1 + 2N_k + N_i$ degrees of freedom in which N_k is the order of the Fourier series and N_i is the number of observation nights. The amplitude of a light curve was calculated after rejecting the upper and lower 5% of data points.

Using the detections of different bands obtained from the first night, the colors can be calculated for the observed asteroids. To remove rotational effect in the color calculation, an offset for each band was simply fitted using Equation (1) with the solution obtained from the rotation period fitting. Therefore, only asteroids with a rotation period of $U >= 2$ have color calculation. However, we rejected a case if its detections in g_{P1}, r_{P1}, i_{P1}, and z_{P1} bands do not follow its folded light curve in the w_{P1} band well. Moreover, we adopted the first-order translation from Tonry et al. (2012) to covert the PS1 color into the Sloan Digital Sky Survey (SDSS) color, and then determined the spectral type using the SDSS color, a^*[6] versus i–z (Ivezić et al. 2002), and the boundary defined by Parker et al. (2008).[7]

Since the phase angles only had a small variation during our relatively short observation time span, a fixed G_w slope of 0.15 in the H–G system was simply applied to estimate the absolute magnitudes of asteroids (Bowell et al. 1989). We then estimated the diameter using

$$D = \frac{1329}{\sqrt{p_v}} 10^{-H_w/5}, \quad (2)$$

where H_v is the absolute magnitude in the V band converted from the H_w from our observation, D is the diameter in km, p_v is the V-band geometric albedo, and 1329 is the conversion constant. We adopted the albedo value for S-, V-, and C-type to be $p_v = 0.23$, 0.35, and 0.06 from DeMeo & Carry (2013) if the asteroid has its spectral-type determination from our

[6] $a^* = 0.89 * (g–r) + 0.45 * (r–i) - 0.57$, which was first used to distinguish blue ($a^* < 0$) and red ($a^* > 0$) asteroids in the SDSS r–i versus g–r diagram (?).

[7] The SDSS colors of C- and X-type (i.e., including the E-, M-, and P-type) are overlapped in the region of $a^* < 0$ (i.e., the neutral color objects; Ivezić et al. 2001; DeMeo & Carry 2013). To distinguish the C- and X-type asteroids, we rely on albedo or the spectrum. In this work, we follow the definition of Parker et al. (2008) to show the diverse colors of our samples.

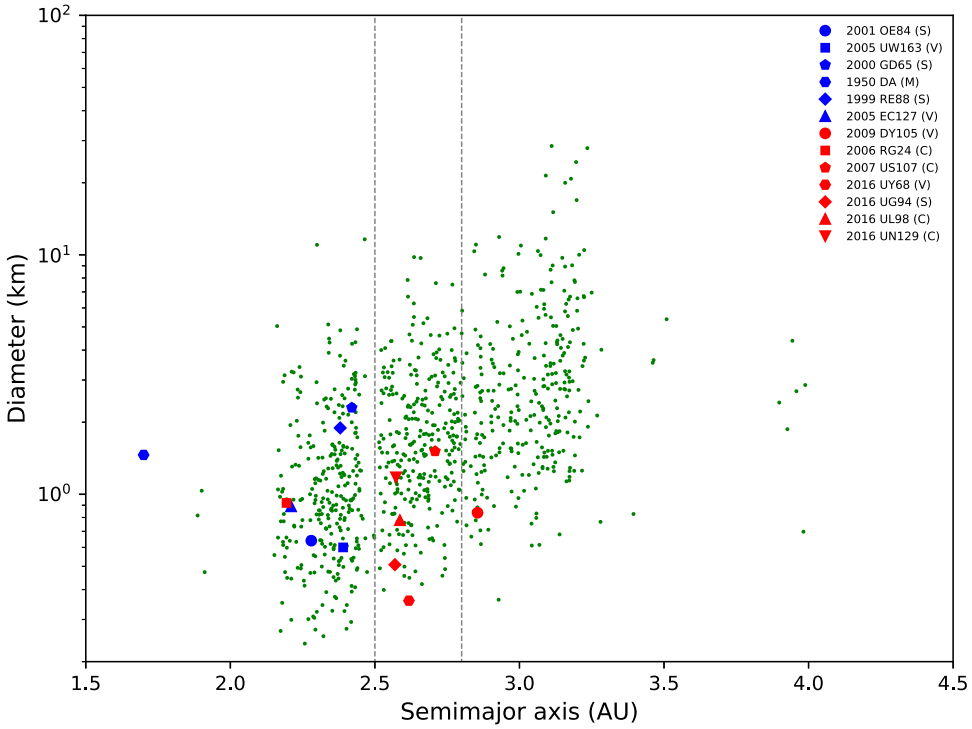

Figure 2. Asteroid diameter vs. semimajor axis. The green filled circles are asteroids with reliable rotation periods, and the gray ones are asteroids with 10 or more detections. The dashed lines show the divisions of empirical geometric albedo in the w_{P1} band used for diameter calculations for asteroids in different locations. The blue and red symbols are the six known SFRs and the seven PS1-SFRs, respectively. Their designations are given on the plot.

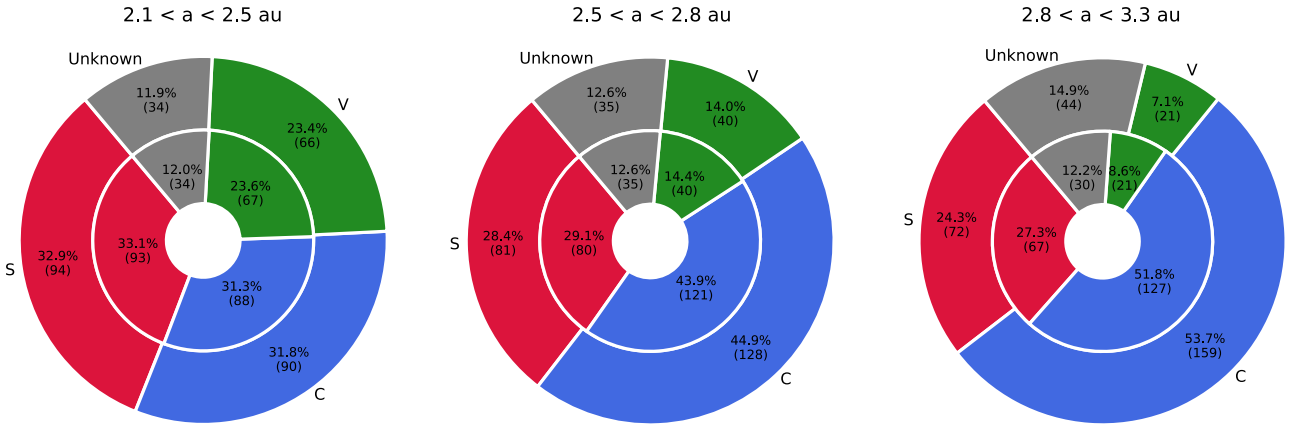

Figure 3. Spectral-type distributions of our samples with qualified color measurements in the inner (left), mid (middle), and outer (right) main belt. The outer annulus includes all sizes, and the inner one is limited to the diameters of $D < 5$ km. The percentage and the number in each bin are give on the plot.

observation. Otherwise, three empirical albedo values, p_w =0.20, 0.08, and 0.04, were assumed for asteroids in the inner ($2.1 < a < 2.5$ au), mid ($2.5 < a < 2.8$ au), and outer ($a > 2.8$ au) main belts, respectively (Tedesco et al. 2005). However, if the *Wide-field Infrared Survey Explorer (WISE)/Near-Earth Object Wide-field Infrared Survey Explorer* (*NEOWISE*) diameter estimation of an asteroid is available, we then adopted that value (Grav et al. 2011; Mainzer et al. 2011; Masiero et al. 2011).

4. Results and Discussion

4.1. The Derived Rotation Periods and Colors

From our survey, 3858 asteroid light curves with 10 detections or more in the w_{P1} band were extracted, in which 876 have reliable measurements for their rotation periods (i.e., $U >= 2$). Their magnitude distribution is shown in Figure 1, where we see that the recovery rate of rotation period is decreasing toward the faint end. Most of our samples are MBAs, and the rest includes some Hungaras, Cybeles, and Hildas. The diameter range of our samples can be found in Figure 2, which shows the plot of their semimajor axes versus diameters. Among the 876 asteroids with reliable rotation periods, 762 have qualified color measurements for spectral-type determinations. Their spectral distributions were divided by the inner ($2.1 < a < 2.5$ au), mid ($2.5 < a < 2.8$ au), and outer ($a > 2.8$ au) main belt and are shown in Figure 3. We see that the C-type becomes more dominant with greater heliocentric distances. The detailed information of 876 asteroids with reliable rotation periods are listed in Table 3, and their folded light curves are shown in Figure 4.

Table 3
The 876 Reliable Rotation Periods

Obj. ID	Designation	a	e	i	$\triangle$	r	α	D	H	m	Period	$\triangle m$	U	a^*	i–z	Type
01489[a]	(1489) Attila	3.20	0.14	2.5	5.1	5.1	5.1	24.4	11.74 ± 0.14	16.50 ± 0.00	11.32 ± 0.11	0.43	3	−0.15 ± 0.00	−0.01 ± 0.01	C
02289[a]	(2289) McMillan	2.64	0.14	2.2	5.6	5.5	5.6	9.8	13.72 ± 0.04	17.65 ± 0.00	4.48 ± 0.04	0.12	2	−0.10 ± 0.01	−0.16 ± 0.01	C
02464[a]	(2464) Nordenskiold	3.18	0.20	0.8	5.0	5.0	4.9	20.8	12.08 ± 0.10	15.35 ± 0.00	5.21 ± 0.01	0.29	3	−0.12 ± 0.00	0.03 ± 0.01	C
02527[a]	(2527) Gregory	2.46	0.19	2.6	5.3	5.3	5.3	11.6	13.35 ± 0.06	15.18 ± 0.00	6.11 ± 0.03	0.18	2	−0.15 ± 0.00	0.01 ± 0.00	C
02574[a]	(2574) Ladoga	2.85	0.07	2.1	4.9	4.9	4.9	11.0	12.00 ± 0.05	15.31 ± 0.00	18.90 ± 0.29	0.23	2	0.10 ± 0.00	−0.10 ± 0.00	S
02712	(2712) Keaton	2.16	0.04	0.8	5.3	5.3	5.3	5.0	13.85 ± 0.05	16.19 ± 0.00	5.87 ± 0.04	0.17	2	…	…	…
03293	(3293) Rontaylor	2.40	0.14	2.1	5.7	5.7	5.7	3.6	14.42 ± 0.09	17.83 ± 0.00	2.90 ± 0.01	0.23	3	0.13 ± 0.01	−0.11 ± 0.01	S
03516	(3516) Rusheva	2.88	0.08	2.3	5.1	5.1	5.1	8.3	12.62 ± 0.09	15.81 ± 0.00	3.53 ± 0.01	0.27	3	0.20 ± 0.00	0.03 ± 0.00	S
03766	(3766) Junepatterson	3.23	0.11	1.5	5.0	5.0	5.0	27.9	11.89 ± 0.04	16.34 ± 0.00	11.27 ± 0.16	0.12	2	…	…	…
04831	(4831) Baldwin	3.09	0.11	0.3	5.2	5.2	5.3	21.4	12.46 ± 0.11	17.15 ± 0.00	5.00 ± 0.02	0.31	3	…	…	…

Notes. Columns: compact IDs, designations, semimajor axis (a, au), eccentricity (e, degree), inclination (i, degree), diameter (D, km), mean heliocentric distance ($\triangle$, au), mean geodesic distance (r, au), mean phase angle (α, degree), diameter (D, km), absolute magnitude (H, mag), apparent magnitude (m, mag in w_{P1}), derived rotation period (hr), light-curve amplitude (mag), rotation period quality code (U), SDSS color $a*$, SDSS color i–z, and spectral type.

[a] Rotation period measurements available in the LCDB.

[b] Long-period objects with partial coverage on rotational phase.

[c] *WISE*/*NEOWISE* diameter.

(This table is available in its entirety in machine-readable form.)

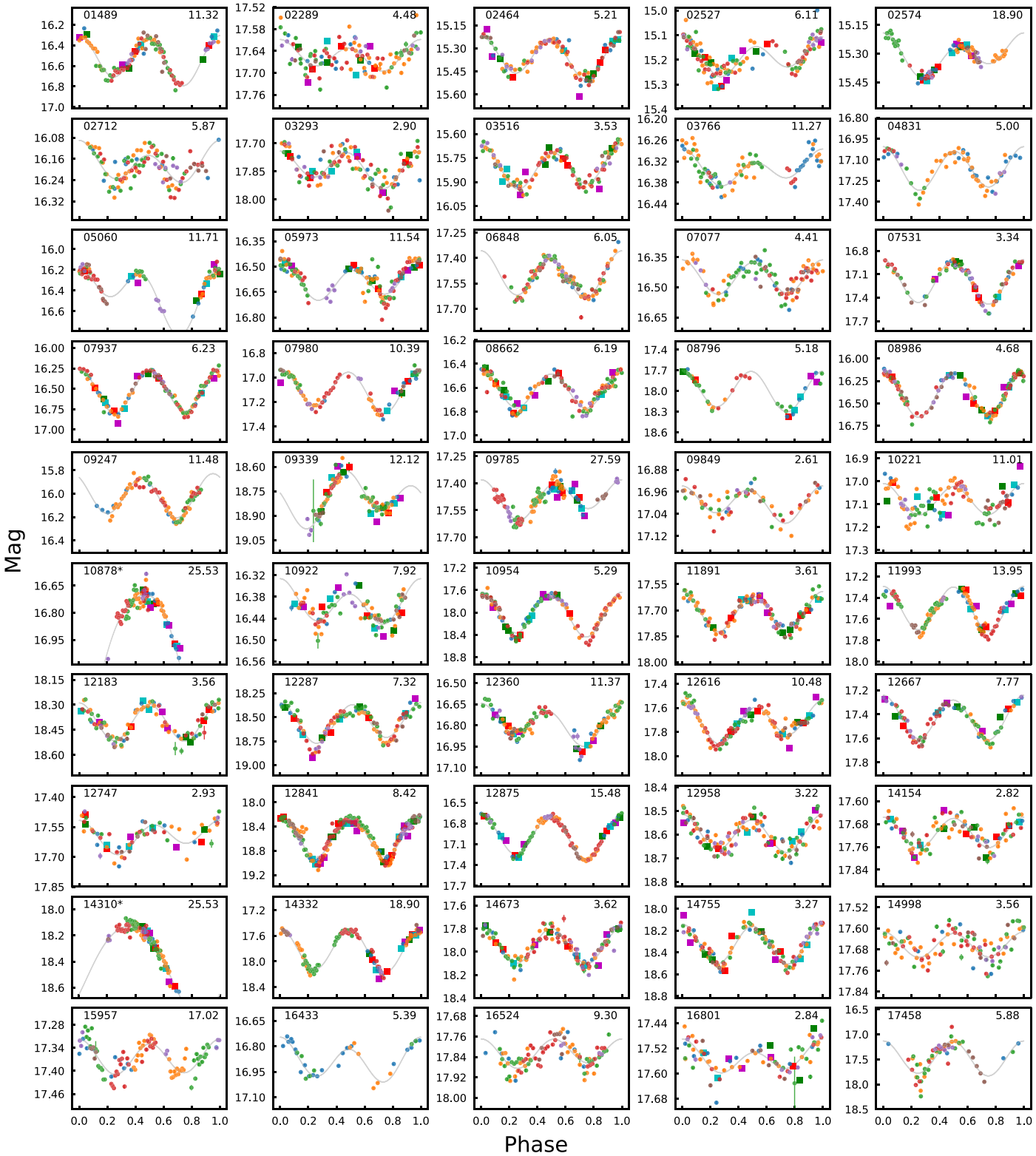

Figure 4. Set of 50 folded light curves for the reliable rotation periods. The filled circles with different colors are data points in the w_{P1} band taken from different nights. The filled squares in green, red, cyan, and magenta are data points in g_{P1}, r_{P1}, i_{P1}, and z_{P1} bands. The compact number/designation of the asteroid is given on each plot along with its rotation period. Note that the data points in g_{P1}, r_{P1}, i_{P1}, and z_{P1} bands are shifted to match the folded light curve in the w_{P1} band. The remaining light curves are available in the figure set.

(The complete figure set (18 images) is available.)

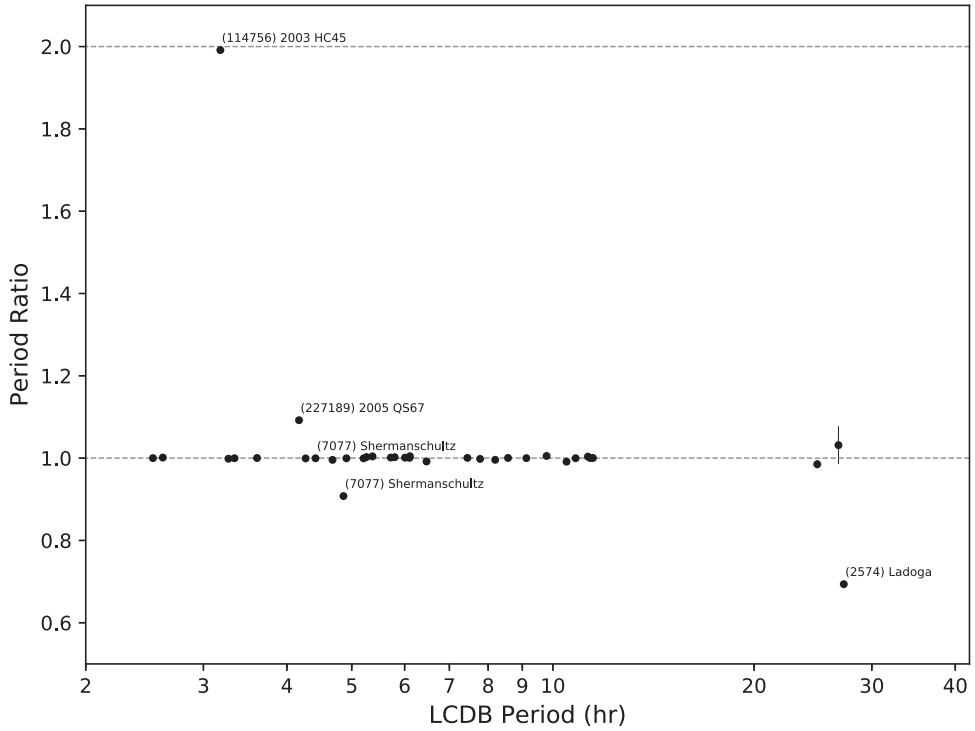

Figure 5. Rotation period comparison for asteroids available in both this work and the LCDB. The rotation period ratios of 34 asteroids are shown in this plot. Note that only $U \geqslant 2$ objects in the LCDB are used in the comparison.

Among the 876 asteroids with reliable rotation periods, 34 of them also have a rotation period of $U \geqslant 2$ listed in the Lightcurve Database (LCDB).[8] Therefore, we compare their rotation periods in both data sets. The ratios of rotation periods from our survey to the LCDB are shown in Figure 5 where we see that most objects have consistent results, except for four objects that show differences greater than 5%. Because our observation time span was only a few days, it was difficult to recover a long rotation period. If possible, we mostly have a folded light curve with partial coverage of a full rotation, like asteroid (2574) Ladoga in Figure 5. Therefore, this kind of a long rotation period obtained from our survey can be seen as a lower limit for these objects. The other three cases are briefly discussed below. For asteroid (114756) 2003 HC45, we derived a rotation period of 6.33 hr, which doubles the value given in Chang et al. (2015). While our folded light curve of 2003 HC45 was assigned as $U = 3$ for its significant double-peak feature, that of Chang et al. (2015) was assigned as $U = 2$ and only shows a single-peak feature with an insignificant secondary dip. Therefore, we believe that Chang et al. (2015) identified half of the actual rotation period for 2003 HC45. For asteroid (7077) Shermanschultz, Waszczak et al. (2015) published two rotation periods, 4.41 and 4.86 hr, using 29 and 28 data points, respectively. Compared to this, our result, 4.41 hr, from a folded light curve of $U = 3$ with many more data points densely covering in the rotational phase is consistent with the former. Therefore, we believe that we have high reliability on the rotation period of (7077) Shermanschultz and that 4.41 hr is the actual value. For asteroid (227189) 2005 QS67, we derived a rotation period of 4.55 hr, which is close to 4.17 hr given by Chang et al. (2015). Both folded light curves were assigned as $U = 2$ and look equally good. Therefore, its rotation period needs further confirmation. Since the difference is less than 10%, we, therefore, see this case as a consistent result. In general, our rotation period measurements are reliable for the following analysis.

4.2. The 2 hr Spin-rate Limit

The 2 hr spin-rate limit shown in the asteroids of $D > 150$ m has been seen as supporting evidence for the rubble-pile structure (Pravec et al. 2002). Although the six large SFRs are shown to be contradictory to the concept of rubble-pile structure, the chance to discover a large SFR is still very rare (see Table 2 in Chang et al. 2017, and the references therein). This is also the case in our survey in which only seven out of the 876 reliable rotation periods were found to be shorter than 2 hr (for a detailed analysis, please see Section 4.3). Figure 6 shows the plot of diameters versus rotation periods of our samples, where we see an obvious stop around 2 hr. Although the chance to find an object with rotation period shorter than 2 hr is higher in our survey (i.e., ∼1%) than in Chang et al. (2015, 2016, i.e., ∼0.1%), the rubble-pile structure is still a reasonable explanation to what we observed.

4.3. The Large SFRs

In our survey, eight objects were found to have reliable rotation periods of <2 hr. Their period analysis was given in Figure 7, in which all the rotation periods are clearly detected on the periodograms and all of the folded light curves show a clean trend. Harris et al. (2014) pointed out that small light-curve amplitude (i.e., less than 0.2–0.3 mag) could possibly be dominated by the fourth or sixth harmonics that lead to a detection of half or one-third of the actual rotation period. To

[8] The LCDB (Warner et al. 2009): http://www.minorplanet.info/lightcurvedatabase.html.

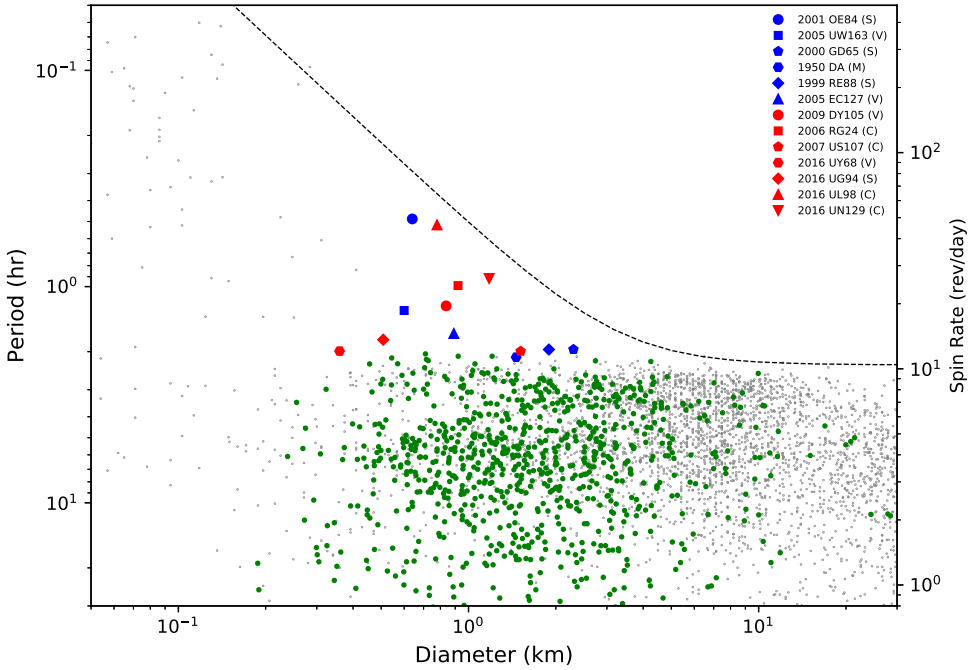

Figure 6. Asteroid rotation period vs. diameter. The green and gray filled circles are the asteroids with reliable rotation periods in this work and the LCDB objects of $U \geqslant 2$, respectively. The six known SFRs are shown with blue symbols, and the seven PS1-SFRs are in red. The dashed line is the spin-rate limit with internal cohesion adopted from Holsapple (2007).

test this possibility, we used the fourth-order Fourier series to run the analysis for these eight objects again. Figure 8 shows the periodograms and the folded light curves of the fourth-order Fourier series fitting, where we see all the fittings have been improved in some way due to the better fitting in the detailed features. The best-fitted periods of the fourth-order fitting are consistent with the previous second-order fitting except for 2001 FQ10 and 2016 UL98 that their best-fitted periods of fourth-order analysis are double the periods of the previous second-order fitting. For 2001 FQ10, its fourth-order folded light curve enhances a very insignificant third peak that was missed in the previous second-order fitting and gives 3.38 hr as the best-fitted period. Therefore, we exclude this objects as an SFR for now and wait for further confirmation of its rotation period. For 2016 UL98, the folded light curve of the fourth-order fitting shows a very insignificant difference in the depths of the first deep and the third deep. However, we doubt this difference is due to the scattered data points. If the difference is true, the new period (i.e., 1.04 hr) is still shorter than 2 hr, and this remains 2016 UL98 as an SFR as well. Therefore, we use 0.52 hr as the rotation period of 2016 UL98 in the following discussion. The detailed information of these seven objects (hereafter, PS1-SFRs) along with the previously reported large SFRs can be found in Table 4.

The diameter range of the PS1-SFRs is from ~0.3 to ~1.5 km.[9] Using $P \sim 3.3\sqrt{(1+\Delta m)/\rho}$, the minimal bulk density to maintain the equilibrium between self-gravity and centrifugal force for a rubble-pile asteroid can be calculated (Harris 1996). Figure 9 shows the plot of the spin rates versus light-curve amplitudes of our samples with the spin-rate limits calculated for bulk densities of $\rho = 3$, 4 and 5 g cm^{-3}, where we see that the PS1-SFRs all need a relatively high bulk density to survive under their super-fast rotations. In addition to the PS1-SFRs, another asteroid of $D \sim 0.7$ km, 2016 UK50, also requires a bulk density of $\rho > 4$ g cm^{-3} to keep intact, although its rotation period is only 2.2 hr. Such a high bulk density is unusual among asteroids (see Table 2 in DeMeo & Carry 2013). Therefore, the PS1-SFRs and 2016 UK50 are very unlikely to be explained simply by the rubble-pile structure. Is it possible that these PS1-SFRs are large monoliths? Although we have no evidence to rule out this possibility totally, the question becomes: how could they avoid numerous collisions or keep these numerous impacts from being destructive?[10]

The color calculations of the PS1-SFRs are shown in Figure 10. Except for 2016 UL98, the color measurements of the other six PS1-SFRs all have good agreements with the folded light curve in the w_{P1} band. Although the color measurements of 2016 UL98 are relatively scattered, they are still within their light-curve variation in the w_{P1} band. In addition, 2016 UN129 might also have great uncertainty in its color measurements because it is relatively faint and has only one detection in each g_{P1}, r_{P1}, and i_{P1} band. Figure 11 shows the plot of the SDSS a^* versus i–z for the seven PS1-SFRs on top of the objects with meaningful color calculations in our survey. Note that we adopt the photometric error for the color uncertainty. As shown, most of our samples populate in the dense region of SDSS-sampled asteroids (see Figure 3 in Parker et al. 2008), and the seven PS1-SFRs have diversity in their colors. Among them, 2016 UN129 has an unusual

[9] The diameters of the PS1-SFRs are estimated based upon the assuming albedos of their spectral types. For the neutral-colored objects (i.e., SDSS $a^* < 0$), the diameter would be reduced by a factor of two when assuming E-type (i.e., 0.45; DeMeo & Carry 2013) instead of C-type. However, this still gives the diameter estimations of four neutral-colored PS1-SFRs of $\gtrsim$0.3 km. The details of spectral types of the PS1-SFRs can be found below.

[10] Given the intrinsic collision probability of MBAs shown by Polishook et al. (2016) as $N_{\rm impacts} = P_i N(>r_{\rm projectile}(r_{\rm target}+r_{\rm projectile})^2)$, where $P_i = 2.85 \times 10^{-18}$ km^{-2} yr^{-1} and $r_{\rm projectile}$ is 16 m (Bottke et al. 1994), the PS1-SFRs would have 10^3–10^4 collisions during 1 Gyr.

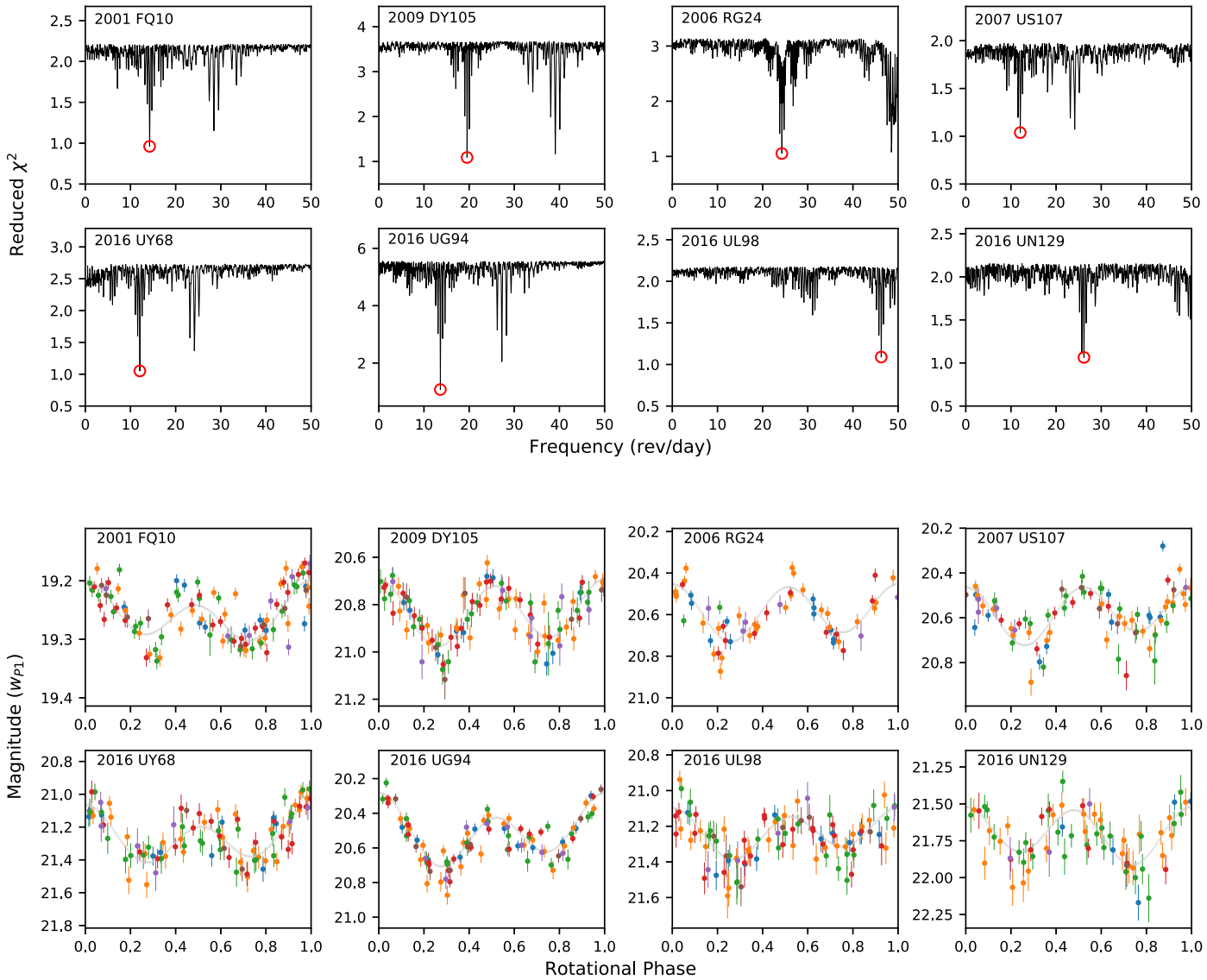

Figure 7. Period analysis for the eight objects of $P < 2$ hr using second-order Fourier series. Top: periodogram; bottom: folded light curve, where colors mean data points taken in different nights.

location on the plot that might be due to its relatively large uncertainty in its colors measurements. Using the boundary defined in Parker et al. (2008), the colors of the seven PS1-SFRs suggest that 2016 UG94 is S-type, 2009 DY105 and 2016 UY68 are V-type, and the other four are C-type.[11] Chang et al. (2017) pointed out a possible taxonomic tendency in the six known large SFRs in which none of them are C-type asteroids. However, the diverse colors of the seven PS1-SFRs seem to rule out that tendency. Although the spectral types of the seven PS1-SFRs need further confirmations, our result suggests that large SFRs in the main belt can have different compositional materials.

Using the Drucker–Prager yield criterion, Holsapple (2007) showed that SFRs can survive with the presence of internal cohesion. Following the equations and calculations shown in Holsapple (2007), Rozitis et al. (2014), Polishook et al. (2016), and Chang et al. (2017), we estimated the cohesion needed for the PS1-SFRs, assuming bulk density $\rho = 2.72$, 1.93, and 1.33 for S-, V-, and C-type, respectively (DeMeo & Carry 2013). The smallest cohesion of the PS1-SFRs is ~10 Pa of 2016 UY68, and the largest is ~700 Pa of 2016 UL98. This cohesion range is similar to that of the known large SFRs (see Table 4) and the lunar regolith (i.e., 100–1000 Pa; Mitchell et al. 1974). This probably suggests a similar source of generating cohesion for these large SFRs.

Unlike the six known large SFRs that belong to either near-Earth objects or inner MBAs, the PS1-SFRs populate throughout the main belt. This suggests that large SFRs can form in any location in the main belt. However, it is very interesting to note that five out of the seven PS1-SFRs are located in the mid main belt. If large SFRs are uniformly distributed in the main belt and have similar sizes (i.e., about 1 km), a general survey for asteroid rotation periods, like ours, should have more chance to discover them in the inner main

[11] Considering that most E-type objects are found in Hungarias and that the population of M-type objects are relatively small in mid main belt (DeMeo & Carry 2013), we believed these four neutral-colored SFRs are very likely to be C-type.

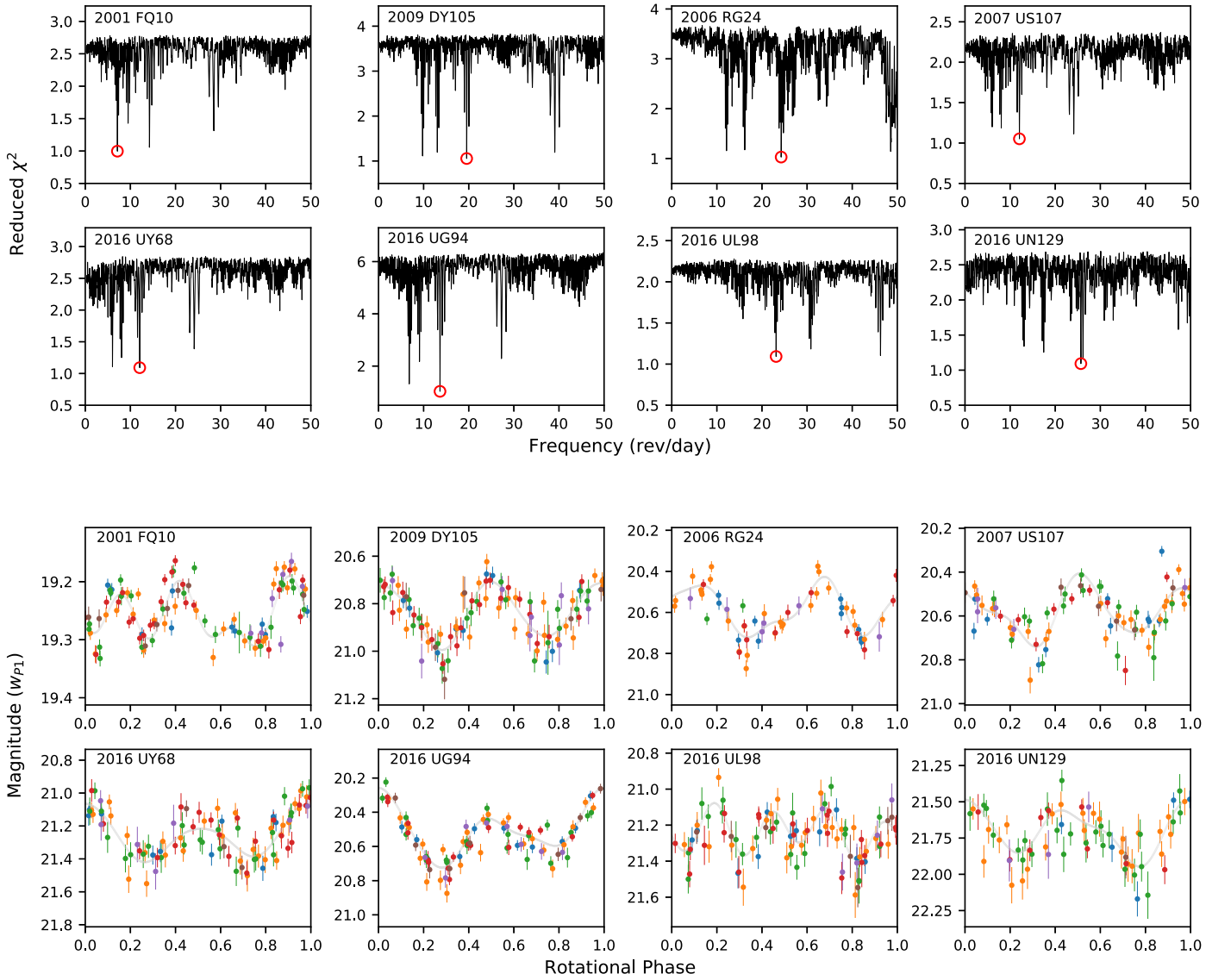

Figure 8. Period analysis for the eight objects of $P < 2$ hr using fourth-order Fourier series. Top: periodogram; bottom: folded light curve, where colors mean data points taken in different nights.

belt (i.e., better photometric accuracy for asteroids with the same size). As shown by the simulation of the deriving rotation period, the chances to recover a spin rate of $f >= 3$ rev day^{-1} are very similar at a fixed magnitude and a fixed amplitude (see Figure 12). Therefore, fewer large SFRs being detected in the inner main belt is not because we missed deriving their rotation periods. Do we obtain more reliable rotation periods in the mid main belt to detect more large SFRs there? When limiting the diameter range to 0.3–2 km, we have 237 and 193 reliable rotation periods in the inner and mid main belt, respectively. Therefore, this is not the case for our survey. A possible explanation is that fewer SFRs exist in the inner main belt. While the detection rate of large SFRs in our survey is only ∼0.4% (i.e., 1 out of 237 reliable rotation periods) in the inner main belt for objects of $0.3 < D < 2$ km, the mid main belt is ∼3.1% (i.e., 6 out of 193). This can also explain why the chance to discover SFRs was lower (i.e., ∼1 out of 1000) in the previous similar surveys (e.g., Chang et al. 2014a, 2015, 2016) than in this work (i.e., ∼1 out of 100). This is because the previous surveys were merely able to detect kilometer-sized asteroids in the mid main belt.

4.4. The Spin-rate Distributions

We first carried out the spin-rate distributions according to their sizes and locations in the main belt. The samples were divided into inner, mid, and outer MBAs with diameters of $3 < D < 15$ km and $D < 3$ km. Moreover, we followed the approach shown by Masiero et al. (2009) and Chang et al. (2015) to consider the possible observational biases in our survey. Figure 12 shows the recovery rates of rotation periods for different magnitudes in the simulation of our survey. In general, it tends to have higher recovery rates for brighter, short-period, and large-amplitude objects. The debiased results are given in Figure 13. Because we only have a small number of asteroids of $3 < D < 15$ km in the inner and mid main belt, we, therefore, exclude them in the following discussion. Overall, our results are very similar to that of Chang et al. (2015).

Table 4
Confirmed Large SFRs to Date

	Asteroid	Tax.	Per. (hr)	Δm (mag)	Dia. (km)	H (mag)	Coh. (Pa)	a (au)	e	i (°)	Ω (°)	ω (°)	References
(395043)	2009 DY105	V	1.23 ± 0.00	0.34	0.8 ± 0.0	17.1 ± 0.1	165.6	2.86	0.04	1.67	190.2	30.6	This work
(475443)	2006 RG24	C	0.99 ± 0.00	0.39	0.9 ± 0.0	18.9 ± 0.1	251.0	2.19	0.21	5.16	221.8	85.5	This work
(476215)	2007 US107	C	1.99 ± 0.00	0.36	1.5 ± 0.1	17.8 ± 0.1	117.8	2.71	0.09	1.50	332.0	46.0	This work
	2016 UY68	V	1.99 ± 0.00	0.49	0.4 ± 0.0	19.0 ± 0.2	9.1	2.62	0.23	3.51	35.9	61.1	This work
	2016 UG94	S	1.76 ± 0.00	0.47	0.5 ± 0.0	18.7 ± 0.1	28.6	2.57	0.21	3.63	40.1	322.4	This work
	2016 UL98	C	0.52 ± 0.00	0.45	0.7 ± 0.0	19.1 ± 0.1	622.2	2.59	0.25	3.34	26.7	314.8	This work
	2016 UN129	C	0.92 ± 0.00	0.55	1.2 ± 0.1	18.3 ± 0.2	573.3	2.57	0.06	4.87	22.0	160.0	This work
(455213)	2001 OE84	S	0.49 ± 0.00	0.5	0.7 ± 0.1	18.3 ± 0.2	∼1500[a]	2.28	0.47	9.34	32.2	2.8	Pravec et al. (2002)
(335433)	2005 UW163	V	1.29 ± 0.01	0.8	0.6 ± 0.3	17.7 ± 0.3	∼200[a]	2.39	0.15	1.62	224.6	183.6	Chang et al. (2014b)
(29075)	1950 DA	M	2.12 ± 0.00	0.2[b]	1.3 ± 0.1	16.8 ± 0.2	64 ± 20	1.70	0.51	12.17	356.7	312.8	Rozitis et al. (2014)
(60716)	2000 GD65	S	1.95 ± 0.00	0.3	2.0 ± 0.6	15.6 ± 0.5	150–450	2.42	0.10	3.17	42.1	162.4	Polishook et al. (2016)
(40511)	1999 RE88	S	1.96 ± 0.01	1.0	1.9 ± 0.3	16.4 ± 0.3	780 ± 500	2.38	0.17	2.04	341.6	279.8	Chang et al. (2016)
(144977)	2005 EC127	V/A	1.65 ± 0.01	0.5	0.6 ± 0.1	17.8 ± 0.1	47 ± 30	2.21	0.17	4.75	336.9	312.8	Chang et al. (2017)

Notes. The values of six known SFRs (i.e., after 2001 OE84) are adopted from Chang et al. (2017).
[a] The cohesion is adopted from Chang et al. (2016).
[b] Δm is adopted from Busch et al. (2007).

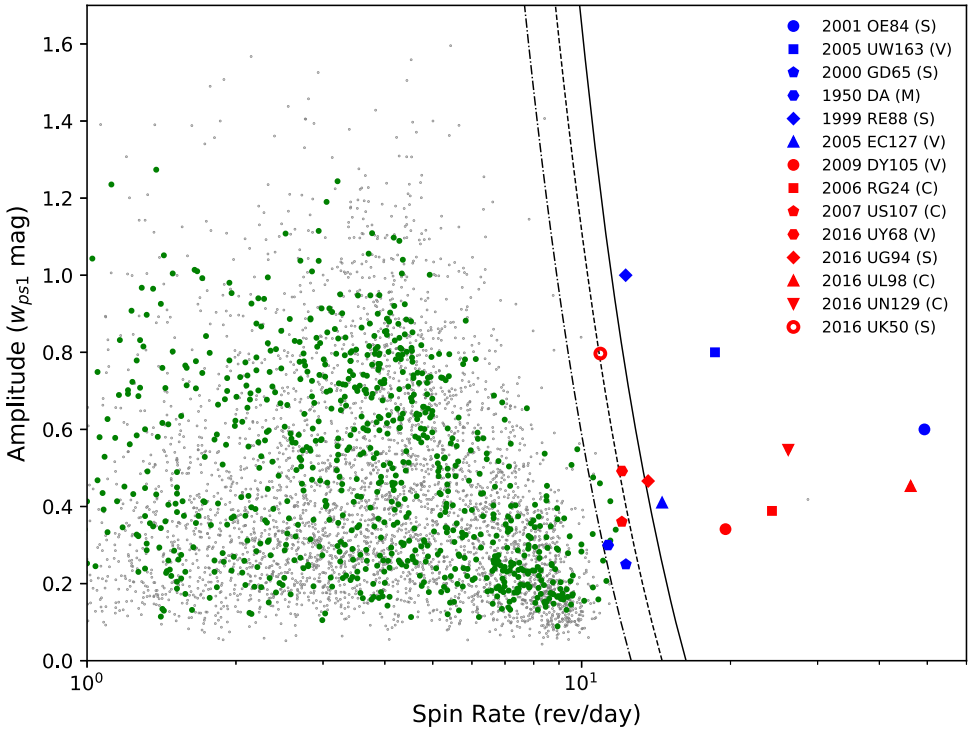

Figure 9. Light-curve amplitude vs. spin rate. The symbols are the same as in Figure 6. The dashed, dotted–dashed, and dotted lines represent the spin-rate limits for rubble-pile asteroids with bulk densities of $\rho = 5$, 4, and 3 g cm^{-3}, respectively, according to $P \sim 3.3\sqrt{(1+\Delta m)/\rho}$ (Pravec & Harris 2000). Note that the asteroids of $D < 0.3$ km are not included in this plot.

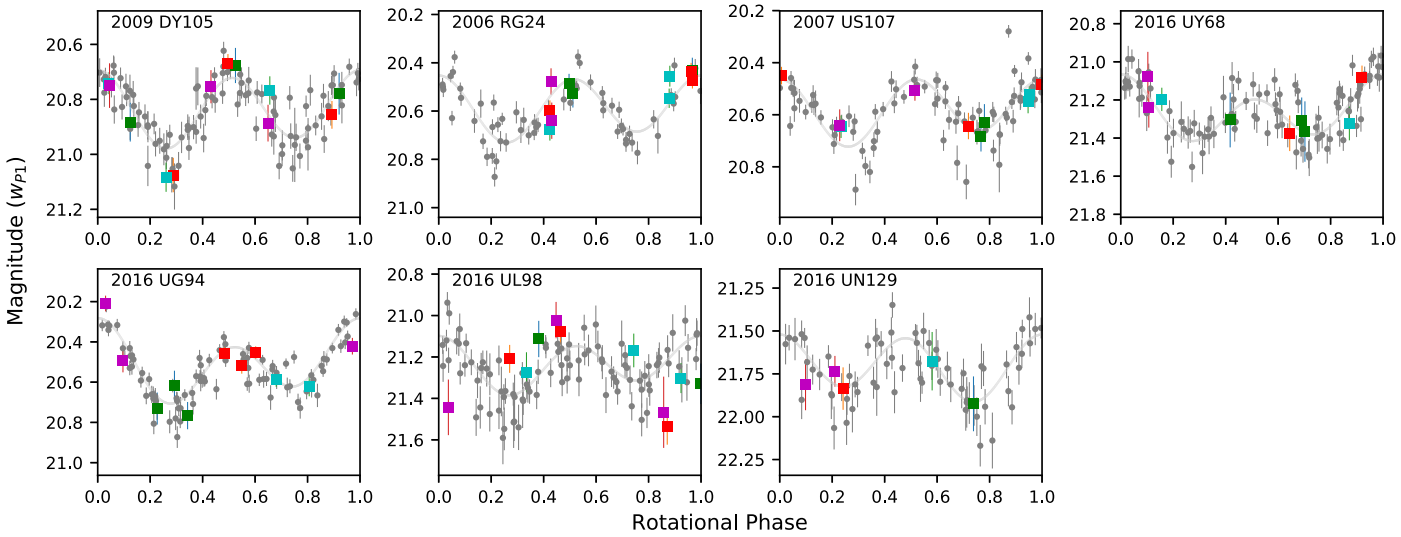

Figure 10. Color calculation for the PS1-SFRs. The gray filled circles are data points in the w_{P1} band. The green-, red-, cyan-, and magenta-filled squares are the data points of g_{P1}, r_{P1}, i_{P1}, and z_{P1}, respectively, and their magnitudes are shifted to match the w_{P1}-band folded light curve.

For asteroids of $3 < D < 15$ km in the outer main belt, we see that the spin-rate distribution shows a smooth decline in the number along the spin-rate. This means that the asteroid system is not in collisional equilibrium; otherwise, it would have a Maxwellian spin-rate distribution (Salo 1987). Although the YORP effect can deviate the distribution from a Maxwellian form, we are not clear how the one like ours can be produced.

For asteroids of $D < 3$ km, a significant drop in the number is observed at a spin-rate of $f = 5$ rev day^{-1} in all locations. As pointed out by Chang et al. (2015), the high spin-rate bins only contain very few small and elongated objects. This is also the case for our survey, in which most fast rotators of $D < 3$ km also have small amplitudes (i.e., <0.4 mag; see the green line in Figure 13). Chang et al. (2015) suspected that the rotational disruption generates the deficiency in small and elongated fast rotators. Because the spin-rate limit for small and elongated objects is lower and their YORP timescales, moreover, are also shorter than large objects, these objects could have been pushed

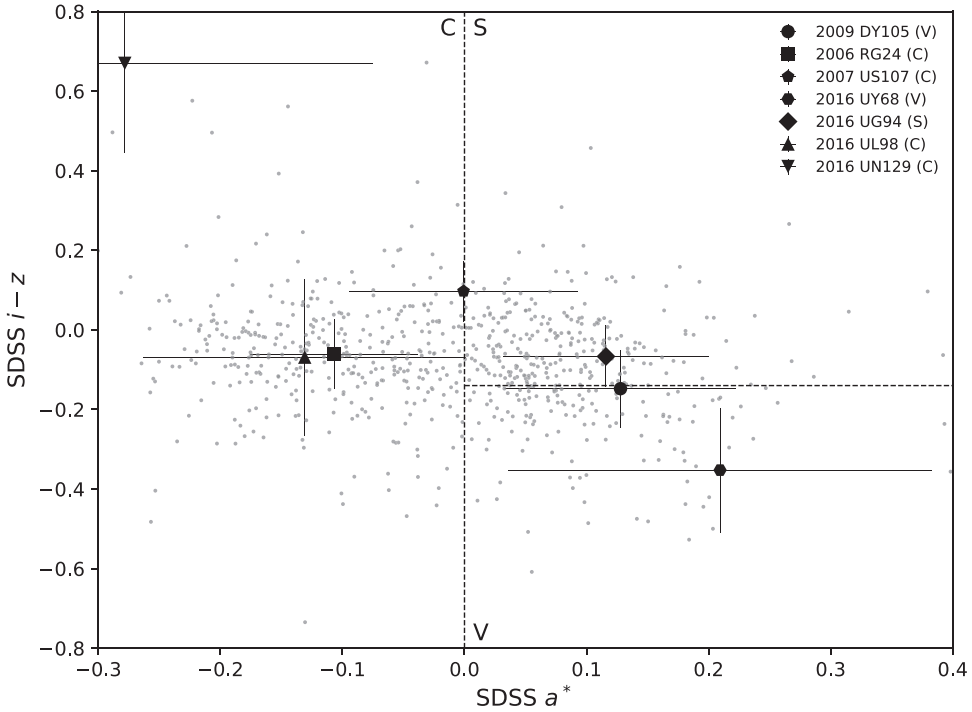

Figure 11. Plot of a^* vs. i–z in SDSS colors for the asteroids with reliable rotation periods and meaningful color calculations. The seven PS1-SFRs are indicated with black symbols with the designation given on the plot. Note that the boundary for S-, C-, and V-type asteroids are adopted from Parker et al. (2008).

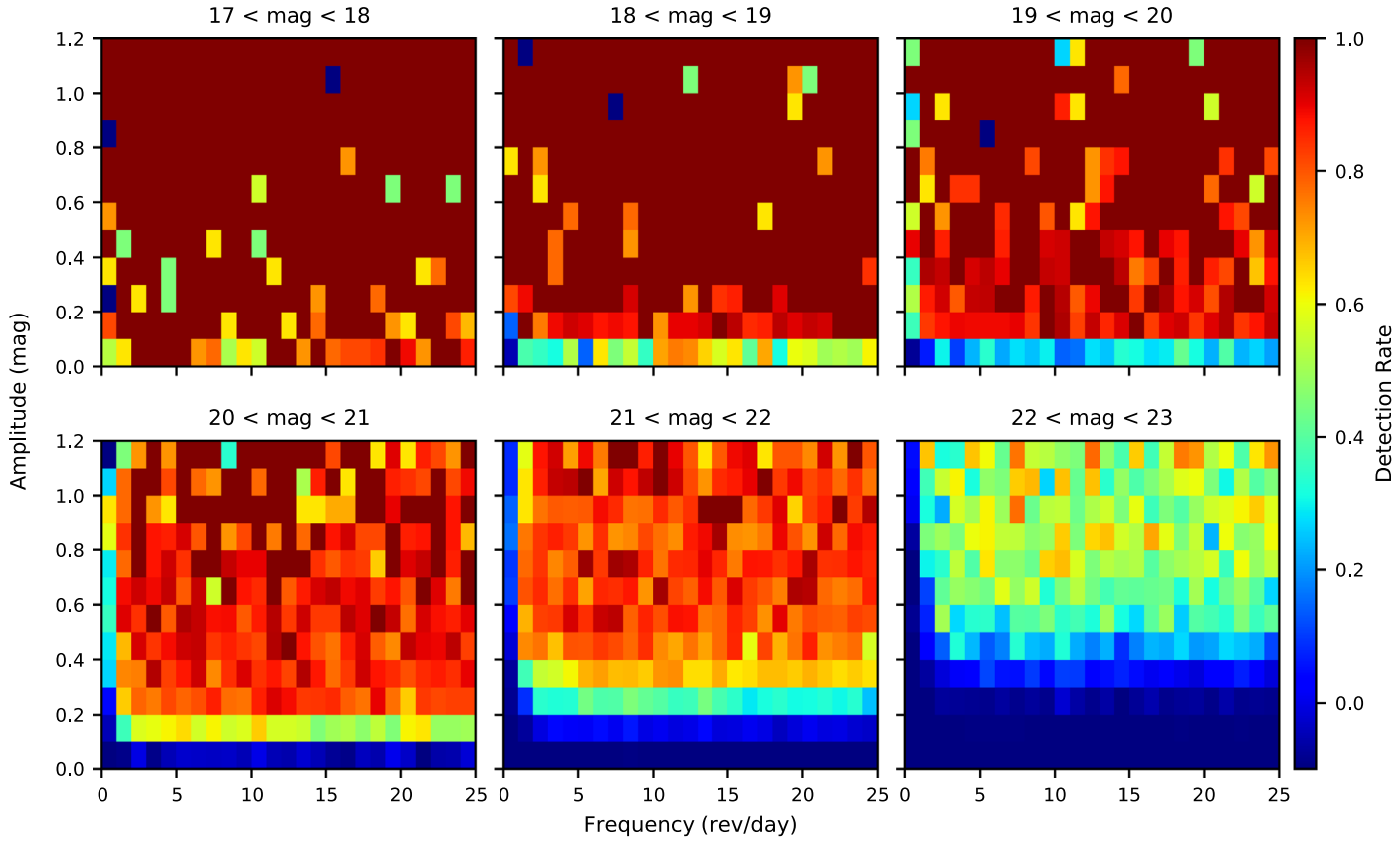

Figure 12. Recovery rate for asteroid rotation period. The color bar represents the recovery rate. The apparent magnitude intervals are given on the top of each plot.

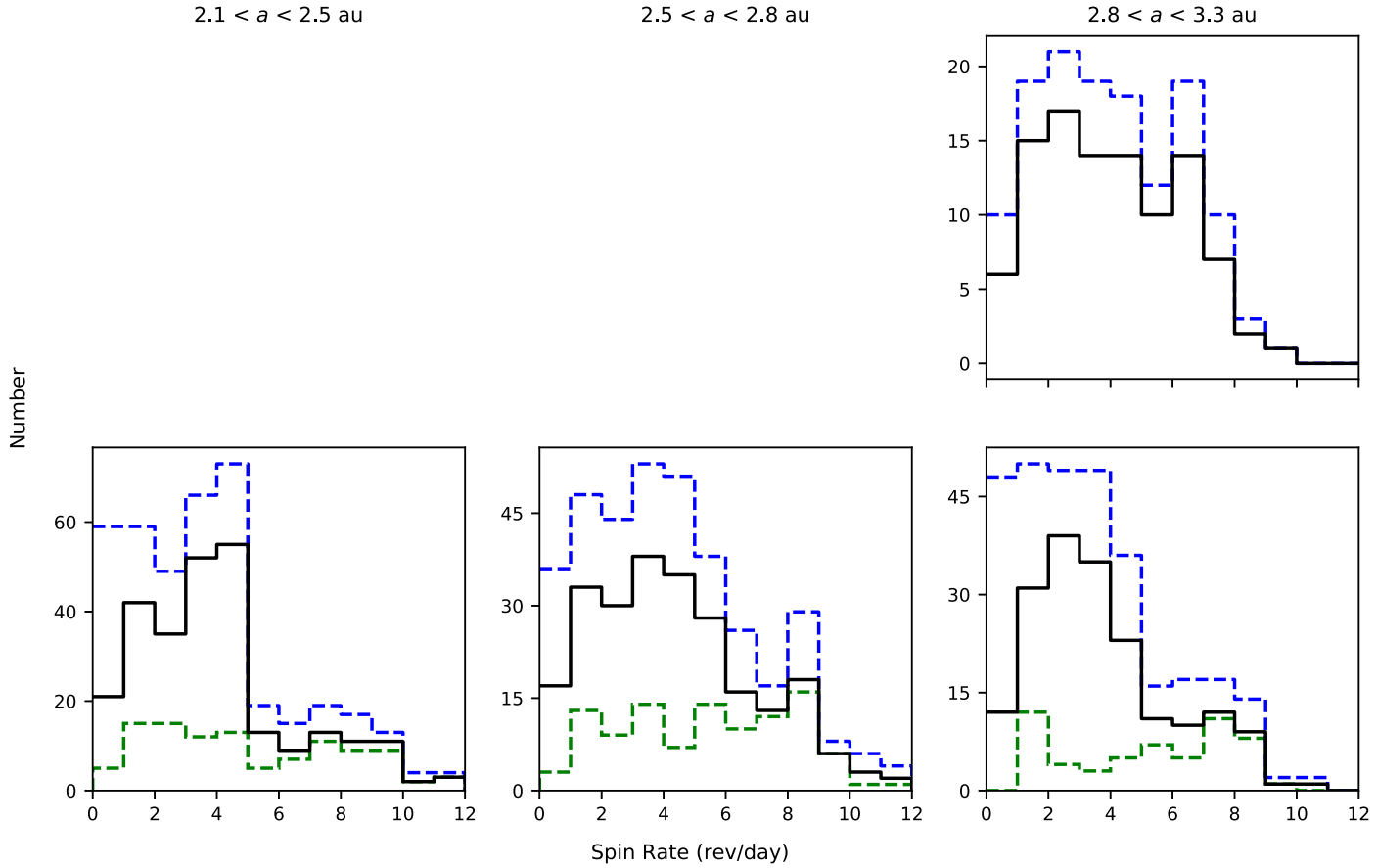

Figure 13. Spin-rate distributions for asteroids with diameters of $3 < D < 15$ km (top) and $D < 3$ km (bottom) in the inner (left), mid (middle), and outer (right) main belt. The black line and blue dashed line are the original distribution and that after debias, respectively. The green dashed line is objects with amplitudes of $\Delta m < 0.4$ mag. Note that the number of asteroids with diameters of $3 < D < 15$ km in the inner and mid main belt are too small to carry out meaningful statistics.

through the spin-rate limit and could have been destroyed already.

Therefore, a comprehensive simulation on the spin-rate evolution for the entire main asteroid belt is needed to understand what we see here.

5. Summary

Using the PS1, we conducted a survey for asteroid rotation periods during 2016 October 26–31, from which more than 1500 new asteroids were reported to the Minor Planet Center, 3858 asteroid light curves with 10 or more detections were extracted, and 876 reliable rotation periods were obtained. The spin-rate distributions for asteroids of different sizes and locations in the main belt are similar to Chang et al. (2015, 2016), which shows that (a) the number of asteroid decreases along with spin rate for asteroids of $D > 3$ km, (b) a number drop appears at $f = 5$ rev day^{-1} for asteroids of $D < 3$ km, and (c) no obvious dependence on the location was found.

Among the 876 reliable rotation periods, only seven objects were found to have rotation periods shorter than 2 hr. This suggests that SFRs are still rare. Considering the significant difference in the number between SFRs and the rest in our survey, it looks like the rubble-pile structure still can explain our observation.

Assuming a rubble-pile structure, the seven PS1-SFRs require relatively high bulk densities to keep intact under their super-fast rotation. Such a high bulk density is unusual among asteroids, and we, therefore, believe other physical strengths, in addition to self-gravity, are needed to explain them. Using the Drucker–Prager yield criterion, the cohesion for the PS1-SFRs was estimated in a range of ~10–600 Pa, which is similar to that of the six known large SFRs and the lunar regolith (Mitchell et al. 1974). This might suggest that SFRs could share a similar source to generate internal cohesion. Unlike the six known large SFRs locating in inner main belt or the near-Earth region, PS1-SFRs populate throughout the main asteroid belt. Moreover, the diverse colors of the seven PS1-SFRs rule out the possible taxonomic tendency previously found in the six known large SFRs. This suggests that the formation of SFR is unlikely to have dependence on location and composition. However, it is interesting that five out of the the seven PS1-SFRs are mid MBAs. Considering the survey condition, we suspect that mid main belt possibly harbors more SFRs than the inner main belt.

This work is supported in part by the National Science Council of Taiwan under the grants *MOST* 107-2112-M-008-009-MY2, *MOST* 104-2112-M-008-014-MY3, *MOST* 104-2119-M-008-024, *MOST* 105-2112-M-008-002-MY3, and also by Macau Science and Technology Fund No. 017/2014/A1 of MSAR. We thank the referee, Dr. Alan Harris, for his useful comments and suggestions to improve the content of this work.

ORCID iDs

Chan-Kao Chang https://orcid.org/0000-0003-1656-4540
Wen-Ping Chen https://orcid.org/0000-0003-0262-272X
K. C. Chambers https://orcid.org/0000-0001-6965-7789

E. A. Magnier https://orcid.org/0000-0002-7965-2815
M. E. Huber https://orcid.org/0000-0003-1059-9603
H. A. Flewelling https://orcid.org/0000-0002-1050-4056
C. Z. Waters https://orcid.org/0000-0003-1989-4879
R. J. Wainscoat https://orcid.org/0000-0002-1341-0952

References

Bottke, W. F., Nolan, M. C., Greenberg, R., & Kolvoord, R. A. 1994, Icar, 107, 255
Bowell, E., Hapke, B., Domingue, D., et al. 1989, in Asteroids II, ed. R. P. Binzel, T. Gehrels, & M. S. Matthews (Tucson, AZ: Univ. Arizona Press), 524
Busch, M. W., Giorgini, J. D., Ostro, S. J., et al. 2007, Icar, 190, 608
Chambers, K. C., Magnier, E. A., Metcalfe, N., et al. 2016, arXiv:1612.05560
Chang, C.-K., Ip, W.-H., Lin, H.-W., et al. 2014a, ApJ, 788, 17
Chang, C.-K., Ip, W.-H., Lin, H.-W., et al. 2015, ApJS, 219, 27
Chang, C.-K., Lin, H.-W., & Ip, W.-H. 2016, ApJ, 816, 71
Chang, C.-K., Lin, H.-W., Ip, W.-H., et al. 2017, ApJL, 840, L22
Chang, C.-K., Waszczak, A., Lin, H.-W., et al. 2014b, ApJL, 791, LL35
DeMeo, F. E., & Carry, B. 2013, Icar, 226, 723
Denneau, L., Jedicke, R., Grav, T., et al. 2013, PASP, 125, 357
Dermawan, B., Nakamura, T., & Yoshida, F. 2011, PASJ, 63, 555
Grav, T., Mainzer, A. K., Bauer, J., et al. 2011, ApJ, 742, 40
Harris, A. W. 1996, LPI, 27, 493
Harris, A. W., Pravec, P., Galád, A., et al. 2014, Icar, 235, 55
Harris, A. W., Young, J. W., Bowell, E., et al. 1989, Icar, 77, 171
Holsapple, K. A. 2007, Icar, 187, 500
Ivezić, Ž., Lupton, R. H., Jurić, M., et al. 2002, AJ, 124, 2943
Ivezić, Ž., Tabachnik, S., Rafikov, R., et al. 2001, AJ, 122, 2749
Kaiser, N., Burgett, W., Chambers, K., et al. 2010, Proc. SPIE, 7733, 77330E
Magnier, E. A., Chambers, K. C., Flewelling, H. A., et al. 2016a, arXiv:1612.05240
Magnier, E. A., Schlafly, E. F., Finkbeiner, D. P., et al. 2016b, arXiv:1612.05242
Magnier, E. A., Sweeney, W. E., Chambers, K. C., et al. 2016c, arXiv:1612.05244
Mainzer, A., Grav, T., Bauer, J., et al. 2011, ApJ, 743, 156
Masiero, J., Jedicke, R., Ďurech, J., et al. 2009, Icar, 204, 145
Masiero, J. R., Mainzer, A. K., Grav, T., et al. 2011, ApJ, 741, 68
McNeill, A., Fitzsimmons, A., Jedicke, R., et al. 2016, MNRAS, 459, 2964
Mitchell, J. K., Houston, W. N., Carrier, W. D., & Costes, N. C. 1974, Apollo Soil Mechanics Experiment S-200, Final Rep. 15 (Berkeley: Univ. California Berkeley)
Parker, A., Ivezić, Ž., Jurić, M., et al. 2008, Icar, 198, 138
Polishook, D., & Brosch, N. 2009, Icar, 199, 319
Polishook, D., Moskovitz, N., Binzel, R. P., et al. 2016, Icar, 267, 243
Polishook, D., Ofek, E. O., Waszczak, A., et al. 2012, MNRAS, 421, 2094
Pravec, P., & Harris, A. W. 2000, Icar, 148, 12
Pravec, P., Harris, A. W., Vokrouhlický, D., et al. 2008, Icar, 197, 497
Pravec, P., Kušnirák, P., Šarounová, L., et al. 2002, ESA Special Publ., 500, 743
Rozitis, B., Maclennan, E., & Emery, J. P. 2014, Natur, 512, 174
Rubincam, D. P. 2000, Icar, 148, 2
Salo, H. 1987, Icar, 70, 37
Sánchez, D. P., & Scheeres, D. J. 2012, Icar, 218, 876
Tedesco, E. F., Cellino, A., & Zappalá, V. 2005, AJ, 129, 2869
Tonry, J. L., Stubbs, C. W., Lykke, K. R., et al. 2012, ApJ, 750, 99
Warner, B. D., Harris, A. W., & Pravec, P. 2009, Icar, 202, 134
Waszczak, A., Chang, C.-K., Ofek, E. O., et al. 2015, AJ, 150, 75
Waters, C. Z., Magnier, E. A., Price, P. A., et al. 2016, arXiv:1612.05245